Numerical Analysis of Deep sub-wavelength integrated plasmonic devices based on Semiconductor-Insulator-Metal strip waveguides

Xiao-Yang Zhang,[1,2] A. Hu,[1,2,3] J. Z. Wen, [3] Tong Zhang, [1,*] Xiao-Jun Xue, [1] Y. Zhou, [3] and W. W. Duley[2]

[1]School of Electronic Science and Engineering, Southeast University, and Key Laboratory of Micro-Inertial Instrument and Advanced Navigation Technology, Ministry of Education, Nanjing, 210096, People's Republic of China

[2] Department of Physics and Astronomy, University of Waterloo, 200 University Avenue West, Waterloo, Ontario N2L 3G1, Canada

[3] Department of Mechanical and Mechatronics Engineering, University of Waterloo, 200 University Avenue West, Waterloo, Ontario N2L 3G1, Canada

** tzhang@seu.edu.cn*

Abstract: We report the first study of nanoscale integrated photonic devices constructed with semiconductor-insulator-metal strip (SIMS) waveguides for use at telecom wavelengths. These waveguides support hybrid plasmonic modes transmitting through a 5-nm thick insulating region with a normalized intensity of 200-300 μm^{-2}. Their fundamental mode, unique transmission and dispersion properties are consistent with photonic devices for guiding and routing of signals in communication applications. It has been demonstrated using Finite Element Methods (FEM) that the high performance SIMS waveguide can be used to fabricate deep sub-wavelength integrated plasmonic devices such as directional couplers with the ultra short coupling lengths, sharply bent waveguides, and ring resonators having a functional size of ≈1 μm and with low insertion losses and nearly zero radiation losses.

OCIS codes: (250.5403) Plasmonics; (250.5300) Photonic integrated circuits; (310.6628) Subwavelength structures; (130.2035) Dispersion compensation devices; (140.4780) Optical resonators.

References and links

1. W. L. Barnes, A. Dereux, and T. W. Ebbesen, "Surface plasmon subwavelength optics," Nature **424**(6950), 824–830 (2003).
2. S. Lal, S. Link, and N. J. Halas, "Nano-optics from sensing to waveguiding," Nat. Photonics **1**(11), 641–648 (2007).
3. V. R. Almeida, Q. Xu, C. A. Barrios, and M. Lipson, "Guiding and confining light in void nanostructure," Opt. Lett. **29**(11), 1209–1211 (2004).
4. A. H. J. Yang, S. D. Moore, B. S. Schmidt, M. Klug, M. Lipson, and D. Erickson, "Optical manipulation of nanoparticles and biomolecules in sub-wavelength slot waveguides," Nature **457**(7225), 71–75 (2009).
5. A. H. J. Yang, T. Lerdsuchatawanich, and D. Erickson, "Forces and transport velocities for a particle in a slot waveguide," Nano Lett. **9**(3), 1182–1188 (2009).
6. B. Desiatov, I. Goykhman, and U. Levy, "Nanoscale mode selector in silicon waveguide for on chip nanofocusing applications," Nano Lett. **9**(10), 3381–3386 (2009).
7. S. Mandal, X. Serey, and D. Erickson, "Nanomanipulation using silicon photonic crystal resonators," Nano Lett. **10**(1), 99–104 (2010).
8. J. Takahara, S. Yamagishi, H. Taki, A. Morimoto, and T. Kobayashi, "Guiding of a one-dimensional optical beam with nanometer diameter," Opt. Lett. **22**(7), 475–477 (1997).
9. T. Nikolajsen, K. Leosson, and S. I. Bozhevolnyi, "Surface plasmon polariton based modulators and switches operating at telecom wavelengths," Appl. Phys. Lett. **85**(24), 5833–5835 (2004).
10. X. Y. Zhang, A. Hu, T. Zhang, X. J. Xue, J. Z. Wen, and W. W. Duley, "Subwavelength plasmonic waveguides based on ZnO nanowires and nanotubes: A theoretical study of thermo-optical properties," Appl. Phys. Lett. **96**(4), 043109 (2010).
11. L. Liu, Z. Han, and S. He, "Novel surface plasmon waveguide for high integration," Opt. Express **13**(17), 6645–6650 (2005).

#130097 - $15.00 USD Received 13 Jun 2010; revised 11 Aug 2010; accepted 12 Aug 2010; published 20 Aug 2010

12. H. T. Miyazaki, and Y. Kurokawa, "Squeezing visible light waves into a 3-nm-thick and 55-nm-long plasmon cavity," Phys. Rev. Lett. **96**(9), 097401 (2006).
13. A. Polman, "Applied physics. Plasmonics applied," Science **322**(5903), 868–869 (2008).
14. A. Hosseini, and Y. Massoud, "Nanoscale surface plasmon based resonator using rectangular geometry," Appl. Phys. Lett. **90**(18), 181102 (2007).
15. Z. Han, V. Van, W. N. Herman, and P.-T. Ho, "Aperture-coupled MIM plasmonic ring resonators with sub-diffraction modal volumes," Opt. Express **17**(15), 12678–12684 (2009), http://www.opticsinfobase.org/oe/abstract.cfm?URI=oe-17-15-12678.
16. R. F. Oulton, V. J. Sorger, D. A. Genov, D. F. P. Pile, and X. Zhang, "A hybrid plasmonic waveguide for subwavelength confinement and long-range propagation," Nat. Photonics **2**(8), 496–500 (2008).
17. R. F. Oulton, V. J. Sorger, T. Zentgraf, R. M. Ma, C. Gladden, L. Dai, G. Bartal, and X. Zhang, "Plasmon lasers at deep subwavelength scale," Nature **461**(7264), 629–632 (2009).
18. R. Salvador, A. Martínez, C. Garía-Meca, R. Ortuño, and J. Martí, "Analysis of hybrid dielectric plasmonic waveguides," IEEE J. Sel. Top. Quantum Electron. **14**(6), 1496–1501 (2008).
19. S. I. Bozhevolnyi, V. S. Volkov, E. Devaux, J.-Y. Laluet, and T. W. Ebbesen, "Channel plasmon subwavelength waveguide components including interferometers and ring resonators," Nature **440**(7083), 508–511 (2006).
20. E. Verhagen, J. A. Dionne, L. K. Kuipers, H. A. Atwater, and A. Polman, "Near-field visualization of strongly confined surface plasmon polaritons in metal-insulator-metal waveguides," Nano Lett. **8**(9), 2925–2929 (2008).
21. J. Tian, S. Yu, W. Yan, and M. Qiu, "Broadband high-efficiency surface-plasmon-polariton coupler with silicon-metal interface," Appl. Phys. Lett. **95**(1), 013504 (2009).
22. P. Nagpal, N. C. Lindquist, S.-H. Oh, and D. J. Norris, "Ultrasmooth patterned metals for plasmonics and metamaterials," Science **325**(5940), 594–597 (2009).
23. E. Moreno, S. G. Rodrigo, S. I. Bozhevolnyi, L. Martín-Moreno, and F. J. García-Vidal, "Guiding and focusing of electromagnetic fields with wedge plasmon polaritons," Phys. Rev. Lett. **100**(2), 023901 (2008).
24. A. V. Krasavin, and A. V. Zayats, "Three-dimensional numerical modeling of photonic integration with dielectric-loaded SPP waveguides," Phys. Rev. B **78**(4), 045425 (2008).
25. O. Tsilipakos, T. V. Yioultsis, and E. E. Kriezis, "Theoretical analysis of thermally tunable microring resonator filters made of dielectric-loaded plasmonic waveguides," J. Appl. Phys. **106**(9), 093109 (2009).
26. V. J. Sorger, R. F. Oulton, J. Yao, G. Bartal, and X. Zhang, "Plasmonic Fabry-Pérot nanocavity," Nano Lett. **9**(10), 3489–3493 (2009).
27. Z. Zheng, M. Iqbal, and J. Liu, "Dispersion characteristics of SOI-based slot optical waveguides," Opt. Commun. **281**(20), 5151–5155 (2008).
28. A. Vial, A.-S. Grimault, D. Macías, D. Barchiesi, and M. L. D. L. Chapelle, "Improved analytical fit of gold dispersion: Application to the modeling of extinction spectra with a finite-difference time-domain method," Phys. Rev. B **71**(8), 085416 (2005).
29. P. B. Johnson, and R. W. Christy, "Optical constants of the noble metals," Phys. Rev. B **6**(12), 4370–4379 (1972).
30. J. E. Toney, "Implementation of a paraxial optical propagation method for large photonic devices," in *Proceedings of the COMSOL Conference Boston 2009*, (unpublished).
31. R. Wan, F. Liu, X. Tang, Y. Huang, and J. Peng, "Vertical coupling between short range surface plasmon polariton mode and dielectric waveguide mode," Appl. Phys. Lett. **94**(14), 141104 (2009).
32. L. Liu, R. Kumar, K. Huybrechts, T. Spuesens, G. Roelkens, E.-J. Geluk, T. de Vries, P. Regreny, D. Van Thourhout, R. Baets, and G. Morthier, "An ultra-small, low-power, all-optical flip-flop memory on a silicon chip," Nat. Photonics **4**(3), 182–187 (2010).
33. T. Carmon, and K. J. Vahala, "Visible continuous emission from a silicamicrophotonic device by third-harmonic generation," Nat. Phys. **3**(6), 430–435 (2007).
34. G. S. Wiederhecker, L. Chen, A. Gondarenko, and M. Lipson, "Controlling photonic structures using optical forces," Nature **462**(7273), 633–636 (2009).
35. F. Zhang, and J. W. Y. Lit, "Direct-coupling single-mode fiber ring resonator," J. Opt. Soc. Am. A **5**(8), 1347–1355 (1988).
36. A. Majkić, M. Koechlin, G. Poberaj, and P. Günter, "Optical microring resonators in fluorineimplanted lithium niobate," Opt. Express **16**(12), 8769–8779 (2008), http://www.opticsinfobase.org/abstract.cfm?URI=OE-16-12-8769.
37. D. Goldring, U. Levy, and D. Mendlovic, "Highly dispersive micro-ring resonator based on one dimensional photonic crystal waveguide design and analysis," Opt. Express **15**(6), 3156–3168 (2007), http://www.opticsinfobase.org/abstract.cfm?URI=oe-15-6-3156.

1. Introduction

Sub-wavelength waveguides are essential components of the next generation of integrated photonic circuits [1,2]. To produce these circuit elements, high-index-contract dielectric waveguides based on nanoslots [3–5] or photonic crystals [6,7] have been developed. An alternative approach is to use plasmonic waveguides involving surface plasmon polariton (SPP) modes with intrinsic metallic properties to generate subwavelength propagation conditions [8]. A variety of such SPP waveguides have been proposed as possible integrated photonic devices in recent years [8–26]. A unique property of these metallic waveguides is

#130097 - $15.00 USD Received 13 Jun 2010; revised 11 Aug 2010; accepted 12 Aug 2010; published 20 Aug 2010

that they can simultaneously carry electronic and optical signals and therefore have the potential to be electronically tunable photonic devices [9,10]. In order to further reduce the size of integrated photonic devices (typically tens of micrometers) to the size of the integrated microelectronic devices (a few micrometers), there is a need to design ultra-compact plasmonic waveguide structures functional over nanoscale dimensions.

Of available SPP waveguides, metal-insulator-metal (MIM) devices [11–15] are expected to best achieve the conditions for compact photonic integration [13]. These waveguide structures produce ultra-high-intensity electromagnetic modes [12] allowing the low radiation loss transmission of optical signals around sharp bends [14,15]. However, the overall propagation loss in these MIM waveguides is enormous due to intrinsic ohmic losses in the metal. This effect becomes more significant when the electromagnetic modes are highly confined to the metal surface. Meanwhile, the high coupling loss with a low energy transfer efficiency presents problems when MIM waveguides are used in the construction of integrated optical devices [15]. To avoid some of these problems, a novel SPP structure was theoretically proposed by Oulton et al. [16]. Such waveguides, working in a hybrid configuration, involve a coupled electromagnetic mode between the bound SPP mode and the optical waveguide mode distributed primarily in a nanoscale region of the low refractive index [16–18]. This hybrid concept is revolutionary and combines the advantages of SPP waveguides with the high-index-contrast dielectric waveguides mentioned above. Compared to conventional MIM modes, hybrid plasmonic modes maintain a volume 100 times smaller than that attainable at the optical diffraction limit while significantly reducing propagation losses. This will help facilitate the design and development of deep subwavelength photonic integrated systems.

In this letter, we present the first study of a vertical and sandwich-shape semiconductor-insulator-metal strip (SIMS) waveguide which is constructed on the surface of a metal film and supports tightly confined hybrid plasmonic modes at ultra high intensities (200-300 μm^{-2}). Different from the hybrid SPP structure proposed by Oulton et al. [16,17], we incorporate a silver strip between the metal film and the insulating gap region. This novel vertically configured waveguide structure, supporting a highly confined SIMS waveguide mode which mainly transmits through the 5-nm thick insulator, is able to reduce the modal radiation losses by ≈70% for sharp bends. Mode wave-guiding and unique dispersion characteristics of the newly proposed structure have been studied theoretically. In addition, we present, for the first time, an analysis of the overall performance of a few fundamental integrated plasmonic devices including a directional coupler, a 90° bend and a ring resonator using three-dimensional (3D) Finite Element Method (FEM). A nearly zero radiation loss is predicted for these integrated devices.

2. Mode properties of the SIMS waveguide

In order to understand the underlying physics of SIMS propagation, we first consider the mode properties with different geometries at a wavelength λ = 1.55 μm (Fig. 1). The cross-section view of our proposed waveguide is shown in Fig. 1(a). It consists of a silicon (refractive n = 3.48) and a silver (n = 0.15 + 11.38i) strip separated by a silicon oxide (n = 1.44) nanosheet with thickness h. The heights of the silicon and silver strips are H_{Si} and H_{Ag}, respectively. These three components all having width W are placed on the surface of a silver film with a thickness more than 200 nm and an infinite width. The strips are surrounded by air (n = 1). This unique high-index and high-contrast configuration in both the x and y directions result in a strong confinement of the electromagnetic mode. Mode distributions and the complex effective refractive index of the hybrid mode N_{eff} are calculated using two-dimensional (2D) FEM eigenmode solver [10,16]. $N_{eff} = N_r + iN_i$ with N_r and N_i corresponding to the real and imaginary parts of this index, respectively. The profiles of the normalized electric field are computed for three different geometries with the variable width W and height H_{Ag}. Vector (shown as arrows) and contour (shown by colors) plots of the normalized E-field for W = 75 nm and H_{Ag} = 200 nm are shown in Fig. 1(b). It indicates that the direction of the E-field in the waveguide is along the y axis (TM-like mode). The profile

#130097 - $15.00 USD Received 13 Jun 2010; revised 11 Aug 2010; accepted 12 Aug 2010; published 20 Aug 2010

of the E-field in the *x* direction presents a nearly uniform distribution in the insulating region. In the *y* direction, it exhibits a high E-field confinement in the insulating region over a nanoscale volume (5nm thick) because of the large discontinuity of the electric field at the interfaces of the high-index-contrast dielectric and the metal. The contour plots of E-fields computed for these three geometries are shown in Figs. 1(c) – (e). In order to present more clearly the mode distributions in the E-field, we define the mode shape [23] in terms of the mode distribution when the electric field amplitude of the mode has fallen to one tenth of its maximum value as shown in Figs. 1(f) – (h). These figures show a clear dependence of mode distribution on waveguide geometry. When $H_{Ag} = 0$, as shown in Fig. 1(f), a large portion of energy expands to the outside the waveguide. This indicates a weak confinement when the mode propagates around a sharp bend in the waveguide and signals the presence of large radiation losses. When H_{Ag} is set to 200 nm, as shown in Figs. 1g and h, energy is distributed closer to the isolating region and the silicon strip. In order to confine more energy in the waveguide itself, the value of *W* can be increased. It is shown in Fig. 1h that more than 80% of the energy modes can be confined within the small area of $\lambda^2 / 35$ when $W = 230$ nm.

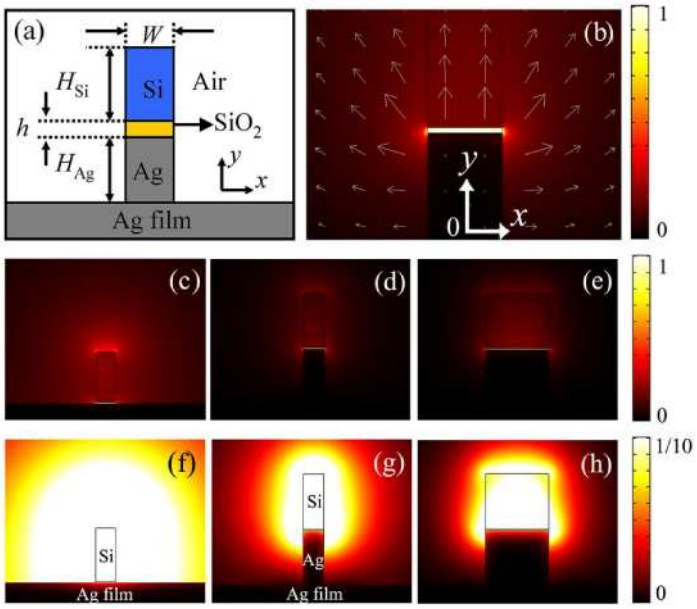

Fig. 1. (a) Schematic diagram of the proposed SIMS waveguide. (b) shows the local |*E*| distribution and the E-field lines of the mode with $W = 75$ nm and $H_{Ag} = 200$ nm. The |*E*| distributions (c)-(e) and the mode shapes (f)-(h) correspond to different geometries. $W = 75$ nm, $H_{Ag} = 0$ nm in (c) and (f), $W = 75$ nm, $H_{Ag} = 200$ nm in (d) and (g), $W = 230$ nm, $H_{Ag} = 200$ nm in (e) and (h).

Figure 2 shows the mode characteristics of the hybrid mode as a function of the height of the silver strip H_{Ag} with different values of H_{Si}. The real and imaginary parts of N_{eff} are shown in Figs. 2(a) and (b), respectively. When $H_{Ag} < 100$ nm the hybrid mode cannot be confined tightly around the strips and energy expands into the interface between the silver film and the air region with a very low mode loss, suitable for applications in low-loss linear waveguides. However, under this condition both the normalized intensity I_{sio2} and the power flow existing in the sandwich strip waveguide P_w are small and therefore the light signal may not be efficiently guided around sharp bends. When $H_{Ag} > 100$ nm, the modes become highly confined to the SIMS waveguide and the value of N_r increases. Under these conditions, the mode distribution is dependent on the heights of the silver and silicon strips. The highest intensity in the insulating gap region is achieved when H_{Si} is nearly 200 nm and 150nm $< H_{Ag} <$ 200 nm as shown in Fig. 2(c). When H_{Si} continues to increase, more energy expands into the silicon strip (as shown in Fig. 2(d)), and I_{sio2} decreases accordingly. Therefore, $H_{Si} = H_{Ag} =$

#130097 - $15.00 USD Received 13 Jun 2010; revised 11 Aug 2010; accepted 12 Aug 2010; published 20 Aug 2010

200 nm are proposed as the optimized heights supporting a high compact mode with the highest intensity density in the insulating gap region, even when W is as small as 50 nm.

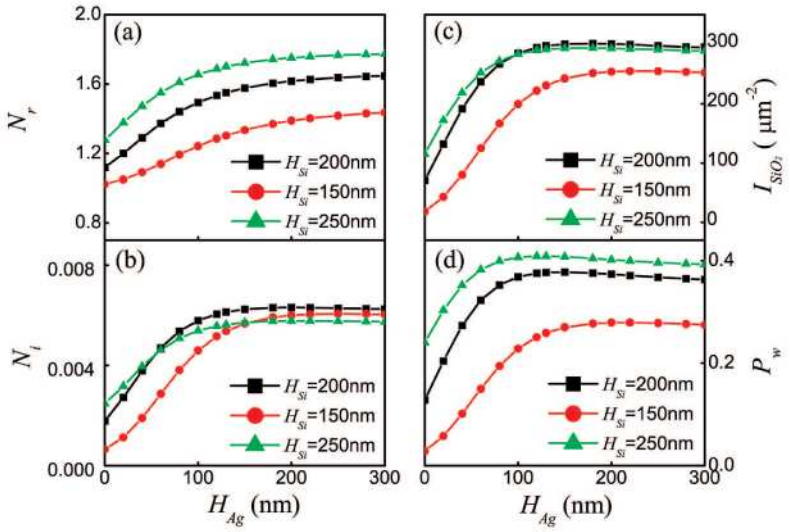

Fig. 2. Mode characteristics of the hybrid mode as a function of the height of the silver strip H_{Ag} with different values of H_{Si}, W = 75 nm and λ = 1.55 μm. The real and imaginary parts of N_{eff} are shown in (a) and (b). The normalized intensity I_{sio2} and the power flow P_w are shown in (c) and (d), respectively.

To study the influence of the thickness (h) of the silicon oxide sheet on the performance of the waveguide, mode characteristic coefficients are calculated for the structures with constant H_{Si} and H_{Ag} as shown in Fig. 3. Figure 3(a) shows values of the normalized average optical intensity I_{sio2} in the SiO_2 nanosheet (left axis) and the power P_w existing in the sandwich strip waveguide (right axis). Here we define $I_{sio2} = P_{sio2} / Wh$, where P_{sio2} is the power in the SiO_2 sheet region [3]. Both P_w and P_{sio2} are normalized with respect to the total waveguide optical power. Generally speaking, a smaller value of h provides a much higher optical intensity and a greater power in the strips. When h = 5 nm, the maximum value I_{sio2} = 300 (μm^{-2}) can be achieved for W = 75nm. It indicates that the light propagation in the SIMS waveguide shows a ultra high intensity (300 μm^{-2}), nearly 5 - 15 times higher than the slot dielectric waveguide (20 - 60 μm^{-2}) and 30 times higher than the silicon-on-insulator (SOI) waveguides (< 10 μm^{-2}) [3]. The curves of P_w represent the energy distribution of the modes in the strip (including the Si, SiO_2 and Ag strips) waveguides. When W is small, more energy expands into the air region. By increasing the value of W to 200 nm, more than 80% of the energy can be confined tightly in the waveguide region for h = 5nm. Figure 3(b) shows the mode propagation length L_p as the function of h and W. Here $L_p = \lambda / (4\pi N_i)$ represents the propagation loss of the modes [10]. As shown, the hybrid mode can propagate almost 20 μm, which is about seven times longer than the length using a MIM waveguide with a similar geometry (after replacing the silver strip with the silicon strip). The propagation length can be increased significantly by decreasing the value of h, however, the intensity I_{sio2} decreases accordingly.

#130097 - $15.00 USD Received 13 Jun 2010; revised 11 Aug 2010; accepted 12 Aug 2010; published 20 Aug 2010

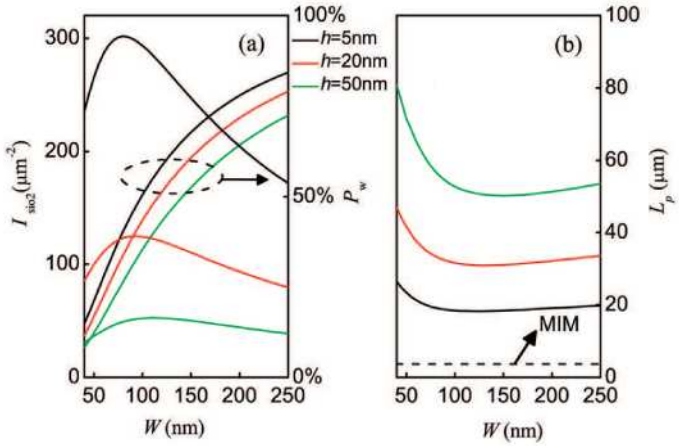

Fig. 3. (a) Normalized average optical intensity I_{SiO2} in a SiO_2 nanosheet and the power P_w existing in a sandwich strip waveguide with different h as a function of W. (b) Propagation length L_p corresponding to different values of h. The dashed line corresponds to the L_p of the MIM waveguide with h = 5 nm. The parameters $H_{Si} = H_{Ag}$ = 200 nm in (a) and (b).

In order to reveal the characteristic of the coupled hybrid modes in depth, we have simulated the mode wavelength dependence as shown in Fig. 4. The refractive indices and material dispersion of the SiO_2 and silicon at optical wavelength range are taken from Ref. 27, and the complex permittivity of the silver is fitted by Drude-Lorentz models [28] using data from Ref. 29. The dispersion of N_r and N_i of the hybrid modes with different W as a function of λ are shown in Figs. 4(a) and (b), respectively. The circular symbols in Fig. 4(a) refer to the minimum wavelength of the mode which can be guided with the single-mode transmission in the SIMS waveguides. As shown in the graphs, both the real part of the effective refractive index and the mode attenuation are seen to increase when λ < 0.7 μm. This results from the significant increases in the optical absorption coefficients of silicon and silver in the short wavelength region. When λ is in the near-infrared, more energy is distributed into the lossless dielectric regions and the mode losses are seen to decrease. So there is a broadband of wavelengths between 0.8 and 2 μm that are suitable for single-mode waveguides combining ultra high intensity and low propagation losses. In this range the modes show a high first-order dispersion because of the high-index-contrast geometries of the SIMS waveguides. For example, When W = 230 nm, N_r can be fitted linearly as $N_r(\lambda) = 4.25 - 1.14\,\lambda$ (μm) with a slope ten times larger than these for conventional plasmonic waveguides and optical waveguides. Such a high first-order dispersion is very useful for improving the performance of resonant devices and will be discussed later. When λ exceeds the range labeled by the dashed line in Fig. 4(b), the mode cannot be confined tightly around the strip waveguide and more energy expands into the air region.

As the SIMS waveguide may work for broadband optical communication and for nonlinear optical applications, we have investigated the higher order dispersion properties of the SIMS waveguides at telecom wavelengths as shown in Figs. 4(c) and (d). The dispersion parameter $D = \frac{d}{d\lambda}(V_g) = -\frac{\lambda}{c}\frac{d^2 N_r}{d\lambda^2}$ represents the second order dispersion effect of the waveguide, where V_g is the group velocity [27]. As shown in Fig. 4(c), by simply changing the width W of the waveguide, D can be tuned with over a wide range between -1.0×10^4, and 0.3×10^4 ps/km-nm. It indicates that the SIMS with a small W has a highly abnormal dispersion regime in which D is two times larger than that for a slot waveguide, and 1-2 orders higher than that in conventional dielectric waveguides [27]. More importantly, when W ≈120 nm there is a low dispersion region at telecom wavelengths as shown in Fig. 4(d). By setting different values of H_{Si}, zero dispersion at certain wavelengths can be achieved. Such unique dispersion characteristics indicate that SIMS waveguides can be used in telecom

#130097 - $15.00 USD Received 13 Jun 2010; revised 11 Aug 2010; accepted 12 Aug 2010; published 20 Aug 2010

communication and optical signal processing systems, e.g., for achieving ultra short pulse, dispersion compensation or broadband signal transmission.

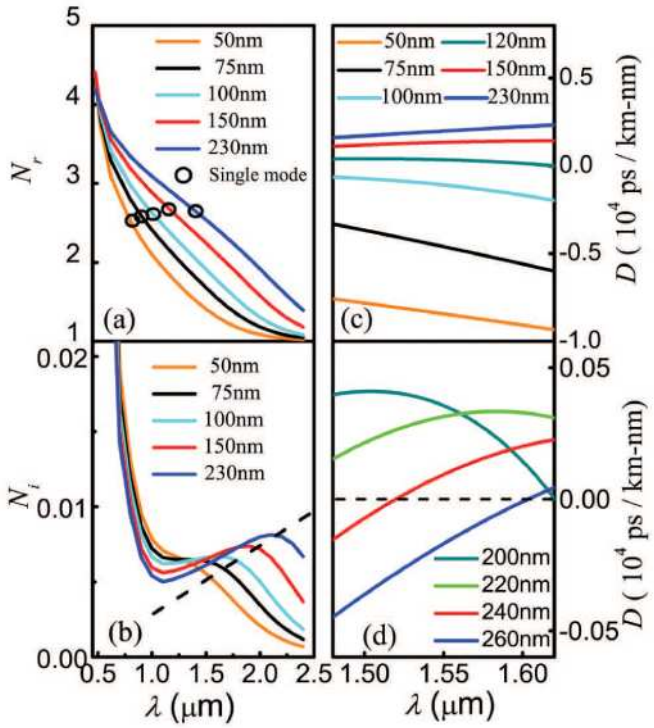

Fig. 4. N_r (a) and the N_i (b) of the hybrid modes with h = 5 nm, H_{Si} = H_{Ag} = 200 nm and different values of W as a function of λ. The circular symbols in (a) refer to the minimum wavelength λ which can support single-mode transmission. The dispersion parameter D at telecom wavelengths corresponds to different values of W with h = 5 nm, H_{Si} = H_{Ag} = 200 nm in (c) and with h = 5 nm, W = 120 nm, H_{Ag} = 200 nm and different values of H_{Si} in (d).

3. Coupling

In addition to the above investigation of the characteristics of a single waveguide, we have further studied some integrated plasmonic devices that can be constructed using SIMS waveguides by rigorous 3D modeling using FEM [24,25]. Our purpose is to investigate the feasibility of developing deep subwavelength photonic integrated circuits based on the new waveguiding structure proposed in this work. The following analyses and discussions, except for certain special examples, are for SIMS waveguides with the parameters h = 5 nm and H_{Si} = H_{Ag} = 200 nm. In order to conduct 3D FEM numerical modeling, we place an absorbing layer at the outer region of the geometries to prevent the reflection of waves [30]. For the outer boundary, the fundamental SPP mode distribution calculated by the 2D eigenmode solver is set as a source boundary condition, and a perfect electric conductor boundary condition with $\mathbf{n} \times \mathbf{E} = 0$ is used at the other boundaries. In the algorithm, non-uniform meshes are adopted to produce convergence and reduce the memory requirement. Finer meshes with a maximum element size of ~1/100 λ – 1/10 λ, and an element growth rate of ~1.2 are used in the sub-domains such as the SiO_2 nanosheet and the silicon and the silver strips. Coarser meshes with a maximum element size of ~1/5 λ – 1/3 λ, and an element growth rate of ~1.3–1.5 are used in the absorbing layer and the air region. We tested the accuracy of our 3D model by comparing the mode propagation lengths of a linear waveguide calculated by the 2D eigenmode solver and the 3D modeling. In comparison with the results of 2D eigenmode analysis, our 3D simulation shows high precision. The comparison of the coupling lengths calculated by the coupled mode theory and the 3D simulation further confirmed the

#130097 - $15.00 USD Received 13 Jun 2010; revised 11 Aug 2010; accepted 12 Aug 2010; published 20 Aug 2010

validity of our 3D model (See the discussion of the coupling effect in Fig. 6). All simulations are conducted using COMSOL Multiphysics software [10,16,30 and 31,].

The evanescent coupling between adjoining two SIMS waveguides at λ = 1.55 μm is studied using coupled mode theory [31] and verified by a full 3D FEM simulation in Figs. 5 and 6. The structure of the coupler is illustrated in Fig. 5(a). The coupled waveguide system support complex in-phase and opposite-phase eigenmodes with propagation constants β_A and β_B, where $\beta_{A,B} = 2\pi N_{rA,B} / \lambda$ respectively. Using coupled mode theory, the coupling length is $L_c = \pi / (\beta_A - \beta_B) = \lambda / 2(N_{rA} - N_{rB})$. Figures 5(b) and (c) show the real and imaginary parts of these eigenmodes as a function of the parameter G. The 2D contours of the in-phase modes and the high-order opposite-phase eigenmodes $|E|$ are shown in Figs. 5(d) and (e) for G = 100 nm, and in Figs. 5(f) and (g) for G = 30 nm, respectively. Figures 5(b) and (c) show that, when the two waveguides are separated by a large distance (G > 50 nm), the difference between the real part N_r of the in-phase and the high order opposite-phase eigenmodes increases with decreasing G. Under this condition, the mode loss of the high order asymmetric mode is only slightly higher than the fundamental mode, so high coupling efficiency with low loss can be obtained. When the gap between the two waveguides continues to decrease (G < 50 nm), the difference between the real part N_r of the two eigenmodes decreases and the mode loss of the high order asymmetric mode suddenly increases. Under these conditions, the coupling efficiency decreases. This occurs because, when the two waveguides are too close together, the E-field of the asymmetric mode is localized in the gap region of the strips (shown in Fig. 5(g)) and more energy dissipates at the surfaces of the metal strips. Thus the optimization of G is a key factor in the design of high performance directional couplers with low insertion losses.

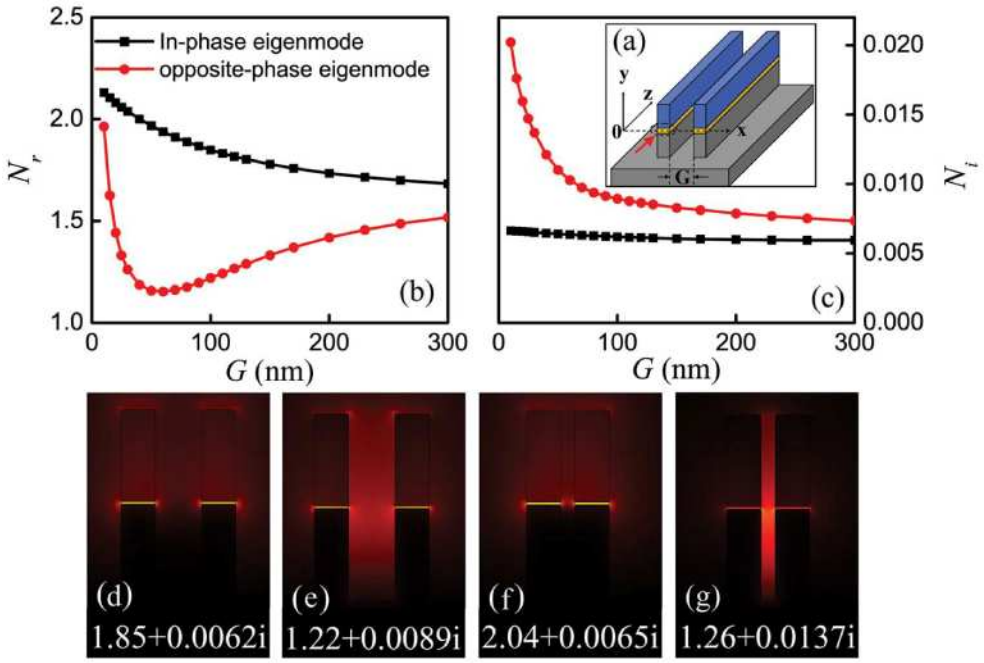

Fig. 5. Calculated eigenmodes of two adjoining SIMS waveguides with W = 75 nm, h = 5 nm, $H_{Si} = H_{Ag}$ = 200 nm and λ = 1.55 μm. (a) Geometry of the SIMS coupler. The real and imaginary parts of the eigenmodes as a function of the parameter G are shown in (b) and (c), respectively. In-phase and the high order opposite-phase eigenmodes $|E|$ with G = 100 nm are shown in (d) and (e). In-phase and the high order opposite-phase eigenmodes $|E|$ with G = 30 nm are shown in (f) and (g). The complex effective refractive index N_{eff} is labeled for each case.

#130097 - $15.00 USD Received 13 Jun 2010; revised 11 Aug 2010; accepted 12 Aug 2010; published 20 Aug 2010

The coupling length L_c as the function of G and W is shown in Fig. 6. Two regions separated by the dashed line show the signal coupling behavior with different coupling efficiency and insertion losses. When G is larger than the value labeled for each W, the signal can be coupled to the other waveguide with high efficiency and relatively low insertion loss (about 7%). When G is relatively small (to the left side of the dashed line in the Figure), the coupling efficiency decreases because both the coupling length and the losses increase significantly. When G is constant, L_c increases with increasing W because the energy mode is confined more tightly for larger W. It should be note that when W = 75 nm and G = 100 nm, L_c is ≈1.2 μm, which is 1 / 18 of the propagation length L_p and less than a wavelength at 1.55 μm in vacuum. In other words, this device behaves as a highly compact directional coupler with a minor coupling loss. The 3D simulation of the signal transmission between two coupled waveguides separated by a distance G = 100 nm is shown in the inset. The graph shows the normalized power flow P at the x-z plane (y = 0 nm) along the z-axis of the waveguides as illustrated in Fig. 5(a). It is clearly observed that the mode energy can be evanescently coupled to the other SIMS waveguide over a much shorter coupling length (in comparison with about 5-30 μm used in the start-of-art plasmonic and optical directional couplers [11,24, and 31,]) and without obvious insertion losses.

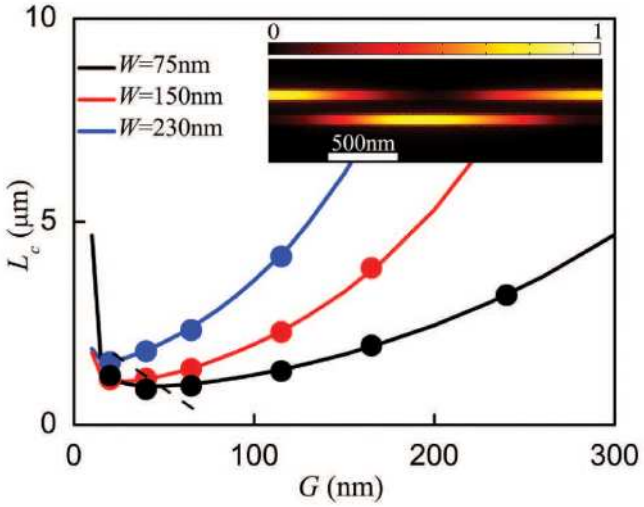

Fig. 6. The calculated coupling length L_c with different W as a function of G by the coupled mode theory (curves) and 3D-FEM simulation (dots) with parameters h = 5 nm and $H_{Si} = H_{Ag}$ = 200 nm at λ = 1.55 μm. The dashed line refers to the minimum value of G corresponding to low loss coupling. Normalized power flow P at the x-z plane (y = 0 nm) along the z-axis of the waveguides with W = 75 nm and G = 100 nm is shown in the inset.

4. 90° Bends

Waveguides having sharp bends are also essential components in highly compact integrated circuits. For these waveguides, in addition to the propagation loss resulting from the imaginary part of the eigenmode, additional insertion losses occurring in a waveguide with a 90° bend are due to radiation and reflection at the sharp corner and that arising from the mode mismatch between the linear and bent waveguides. We calculate the transmission T_b along a 90° waveguide, where $T_b = P_{out} / P_{in}$, and P_{out} and P_{in} are the power flow integrals at the output and input ports of the waveguide, respectively. These bent waveguides have radius R and are 3 μm in length. 3D simulations of the 90° waveguides with different geometries (i.e., varying R, W and H_{Ag}) are carried out for λ = 1.55 μm and are shown in Fig. 7. Figure 7(a) shows the relationship between the radius R and the transmission T_b with different geometries. It is evident that by adding a silver strip of height H_{Ag} = 200 nm, the T_b of the bent SIMS waveguide is much higher than that of a hybrid plasmonic waveguide without a

#130097 - $15.00 USD Received 13 Jun 2010; revised 11 Aug 2010; accepted 12 Aug 2010; published 20 Aug 2010

silver strip. With an optimized value for W, signals can be transmitted through a 90° bend with a large curvature (R = 200 nm) with a relatively low loss. The dashed line represents the transmission T_b (about 0.87) of a 3 μm linear waveguide which has only propagation losses. It indicates that when the radius R is larger than 1 μm, the transmission T_b of the SIMS waveguide is almost the same as for a linear waveguide. Figures 7(b) – (d) show the normalized value ($|\mathrm{Re}E_y|^2$) for the 90° waveguide with R = 200 nm as it varies with W and H_{Ag}. In order to present the radiated energy from these bends more clearly, we adjusted the scale of the color bar of ($|\mathrm{Re}E_y|^2$) to a smaller range (from 0 to 1/200). The processed results for Figs. 7b-d are shown in Figs. 7(e) – (g), respectively. Figures 7(b) and (e) show an optimized geometry with W = 150 nm and H_{Ag} = 200 nm. This waveguide exhibits an ultra small insertion loss of 20% (only 7% larger than that of the linear waveguide) and most energy can be transferred from the input port to the output port. When W is increased to 230 nm (Figs. 7(c) and (f)), the energy mode is confined to the corner region and the insertion loss increases correspondingly. Figures 7(d) and (g) show that, the energy of the modes cannot be confined tightly around the waveguide when the height of silver strip H_{Ag} is 0 and W is small (as 75 nm). With this structure, there is strong radiation loss of energy at the sharp corner and only 10% of the incident energy can be transferred to the output port. The radiation loss is enormous (about 70% greater than the loss for the optimized geometry). From the above comparison, one can see clearly that, the radiation loss at the sharp corner can be suppressed efficiently by incorporating a 200 nm-height silver strip into the hybrid waveguide.

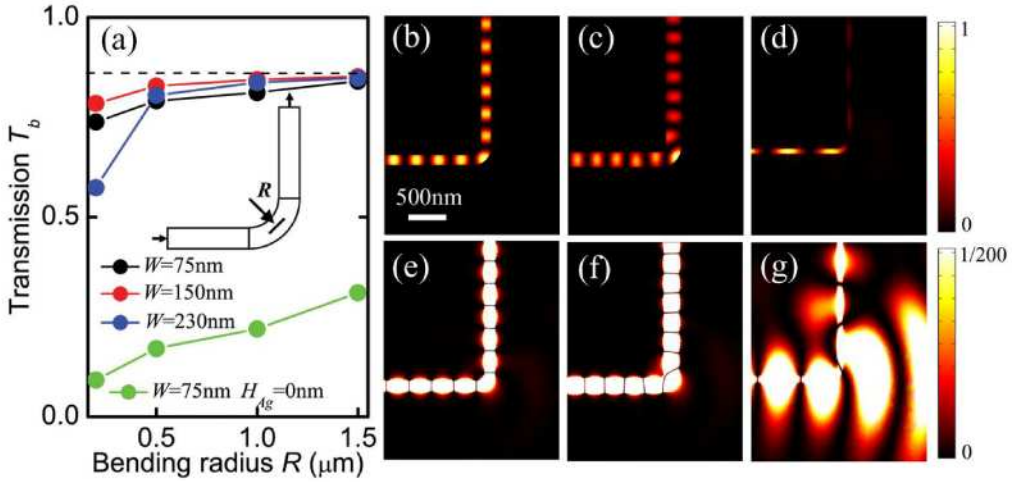

Fig. 7. Comparison of 3D simulations of the 90° bends with different geometries at λ = 1.55 μm. (a) Calculated transmission T_b with different geometries as a function of the radius R. The dashed line represents the transmission T_b of a 3 μm linear waveguide. Comparisons of $|\mathrm{Re}E_y|^2$ of the 90° bends with h = 5 nm, R = 200 nm and W = 150 nm and H_{Ag} = 200 nm in (b) and (e), W = 75 nm and H_{Ag} = 200 nm in (c) and (f), and W = 75 nm and H_{Ag} = 0 nm in (d) and (g).

5. Ring resonator

5.1 Transmission and resonant spectra

Optical ring resonators can be used in optical filters, modulators and switches for high-speed optical communication devices and have great potential for developing active laser cavities and nonlinear as well as optomechanical components [32–34]. In this study, we use the proposed SIMS waveguide to construct a ring resonator with an ultra small radius (R = 500 nm). ($|\mathrm{Re}E_y|^2$) is computed for ring resonators with W = 230 nm and 75 nm at their optimized resonant conditions [35] and is shown in Figs. 8a and b. It is apparent that the electromagnetic mode can be efficiently localized in the resonant cavity when W = 230 nm (Fig. 8(a)) and the resonant intensity in the ring cavity is much higher than the input E-field intensity. When W decreases to 75 nm (Fig. 8(b)), the resonant intensity in the cavity decreases apparently. This

#130097 - $15.00 USD Received 13 Jun 2010; revised 11 Aug 2010; accepted 12 Aug 2010; published 20 Aug 2010

occurs because more energy radiates from highly curved waveguides. The energy radiation loss from this waveguide is illustrated in Fig. 8(c) where the maximum value of the energy mode ($|\mathrm{Re}E_y|^2$) is reduced to 1 / 200.

Transmission and resonant spectra of ring resonators under optimized conditions with different values of W = 75, 150 and 230 nm are simulated in Figs. 8(d) and (e), respectively. The parameter G is set to be 115, 90 and 50 nm corresponding to the critical coupling ratio as defined elsewhere [35]. The optimized condition represents that in which the ring resonator works under the critical coupling ratio with the maximum resonant intensity in the ring cavity. Spectra determined by 3D-FEM simulations (marked by dots) are fitted analytical using Eq. (1) – (2) (solid-lines).

The intensity ratios at the output port and in the ring cavity can be expressed as follows [35],

$$\left|E_{out} / E_{in}\right|^2 = T_l(1-r_0)\left[1-\frac{k(1-k-A)/(1-k)}{1+A-2A^{1/2}\cos(2\pi R\beta_r)}\right] \quad (1)$$

$$\left|E_{ring} / E_{in}\right|^2 = \frac{(1-r_0)k}{1+A-2A^{1/2}\cos(2\pi R\beta_r)} \quad (2)$$

A factor T_l has included in Eq. (1) to allow for the fact that SIMS are lossy waveguides. $T_l = e^{-2\alpha L}$ represents the propagation loss for light from the input to the output ports of the bus waveguide. $L \approx 3$ μm, r_0 is the intensity insertion loss of the coupler, $\alpha = 2\pi N_i / \lambda$ is the amplitude attenuation coefficient, $A = (1-k)(1-r_0)e^{-4\alpha_r \pi R}$ and α_r and β_r are the amplitude attenuation coefficient and the propagation constant of the bent waveguide in the ring resonator, respectively. Here the values of k, α_r and β_r are all dependent on λ and W.

In order to fit the 3D simulation accurately, k, α_r and β_r in Eq. (1) – (2) are taken to be wavelength dependent variables. The parameters k and α_r can be expressed by Eq. (3) – (4)

$$k(\lambda) = k_0(1+e^{(\lambda-u)/v}) \quad (3)$$

$$\alpha_r = 2\pi N_{ir} / \lambda = 2\pi N_i(1+e^{(\lambda-u)/v}) / \lambda \quad (4)$$

where the parameters u and v are chosen to match the 3D plots, N_{ir} and N_i represent the imaginary part of the mode effective index for curved and linear waveguides, respectively.

The dispersion of curved waveguides β_r in the ring cavity is also found to be different from that in linear waveguides. The analytical curves are well matched with the 3D-FEM simulations with the correct set of parameters. It should be noted that, the coupling insertion loss r_0 of the SIMS ring resonators is only 1% ~2%, and is much smaller than that for MIM ring resonators [14,15].

#130097 - $15.00 USD Received 13 Jun 2010; revised 11 Aug 2010; accepted 12 Aug 2010; published 20 Aug 2010

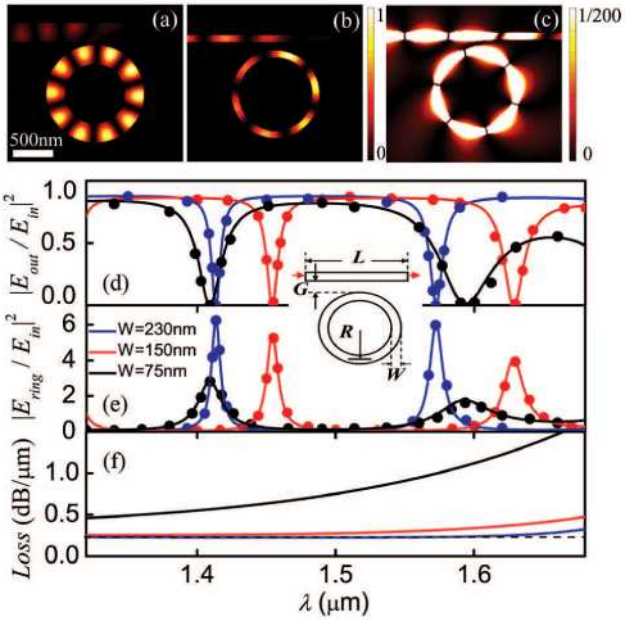

Fig. 8. Simulation of the SIMS ring resonators with R = 500 nm, h = 5 nm and $H_{Si} = H_{Ag}$ = 200 nm. The distribution of the ring resonators with W = 230 nm and G = 50 nm in (a) and W = 75 nm and G = 115 nm in (b). By downscaling the maximum value to 1/200 of the, the energy radiation of the ring cavity with W = 75 nm and G = 115 nm are shown in (c). Calculated transmission spectra, resonant spectra and the loss in ring resonators under optimized conditions with different values of W are shown in (d) - (f), respectively. The dots in (d) and (e) represent the 3D simulation results. The dashed line in (f) corresponds to the propagation loss in linear SIMS waveguides with W = 230 nm.

Wavelength dependent spectra show that the resonant intensity and the notch property of the ring resonators are highly dependent on the value of W. When W = 75 nm, the resonant intensity in the ring cavity is not high and the notch band in the transmission spectrum is wide, especially at longer wavelengths because of the large radiation losses in the cavity. By increasing the value of W, the radiation losses decrease significantly, and when W = 230 nm, an extremely narrow notched band combined with high resonant intensity (six times higher than the input light signal) can be achieved.

To highlight the properties of mode confinement in curved SIMS waveguides, we show analytical fits to wave-guiding losses in the ring waveguides with R = 500 nm and different values of W in Fig. 8(f). The losses in the waveguides of the ring cavity are measured in dB/μm and are given by $Loss = -10\log_{10}(-2\alpha_r)$. The dashed line in Fig. 8(f) corresponds to the propagation loss in linear SIMS waveguides. Unlike in the 90° waveguides, signal energy losses in the ring cavity only include losses due to propagation and the additional radiation loss induced by the ring waveguide at large curvature. We find that radiation losses in the ring cavity SIMS waveguide with W = 230 nm are almost zero. This indicates that by increasing W the mode can be tightly confined tightly to the strip waveguide, almost eliminating radiation losses.

5.2 Highly dispersive property of the SIMS based ring resonator

Highly dispersive ring resonators are very attractive components used in optical communications as well as for sensing applications [36]. In this section, we will show that the proposed SIMS based ring resonators have a unique dispersive property which is ten times higher than the properties of the ring resonators constructed from MIM and conventional dielectric waveguides.

#130097 - $15.00 USD Received 13 Jun 2010; revised 11 Aug 2010; accepted 12 Aug 2010; published 20 Aug 2010

From the spectra shown in Figs. 8d and e, it can be observed that the free-spectral range (*FSR*) $\Delta\lambda_{FSR}$ of the SIMS ring resonator is much narrower than in a MIM resonator with the same radius [15]. This results from the high N_r value and high first-order dispersion nature of the SIMS waveguide. By fitting the 3D plots analytically, we can derive the wavelength dependent N_r simultaneously. The wavelength dependent N_r of the curved waveguides was fitted linearly as follows,

$$N_r = N_0 + b(\lambda - \lambda_0) \tag{5}$$

where λ_0 is a reference wavelength, b refers to the slope of the curves, and N_0 corresponds to the real part of the mode effective index at λ_0. When λ_0 is set to be 1.575 μm, (N_0, b) with W = 75, 150 and 230 nm can be fitted as (1.557, −1.47), (2.1495, −1.37) and (2.5045, −1.24), respectively.

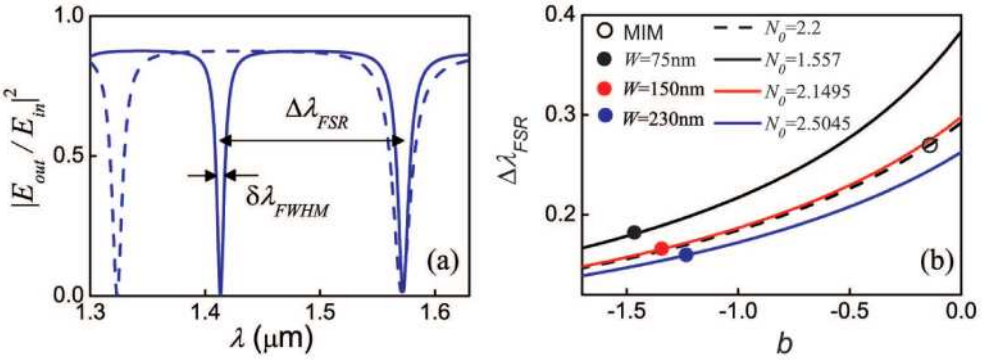

Fig. 9. (a) A comparison between transmission spectra of ring resonators based on waveguides having different dispersions. The structural parameters with the exception of b are chosen from the SIMS ring resonator with W = 230 nm and R = 500 nm. The solid line and the dashed line represent ring resonators with (N_0, b) = (2.5045, –1.24) and (2.5045, –0.124), respectively. (b) The relationship between the $\Delta\lambda_{FSR}$ and the dispersion of the waveguides. The dots refer to the $\Delta\lambda_{FSR}$ of the SIMS ring resonator with different W and the MIM ring resonator.

The contribution of a highly dispersive SIMS waveguide to the transmission spectrum of a ring resonator is illustrated in Fig. 9. We assume that the losses, coupling ratios and the radius of the two ring resonators are the same. Also, N_0 corresponds to the resonant wavelength λ_0 = 1.575 μm and only the slope b of the two cavity waveguides are different. From the comparison transmission spectra as shown in Fig. 9(a), one can see clearly that using highly dispersive SIMS waveguides (solid line) makes both the *FSR* $\Delta\lambda_{FSR}$ and the spectral width of resonances $\delta\lambda_{FWHM}$ (defined in Ref. 37) in the transmission spectrum become narrower. The relationship between $\Delta\lambda_{FSR}$ and waveguide dispersion is shown in Fig. 9(b). $\Delta\lambda_{FSR}$ becomes much smaller when b and N_0 increase. The dots show the *FSR* of SIMS ring resonators with different W as indicated in Fig. 8 and for the MIM ring resonator described in Ref. 15. Although N_0 is almost the same for the MIM ring resonator and for the SIMS ring resonator (W = 150 nm), values of the *FSR* are completely different. This is because the slope (b ≈0.12) of the MIM waveguide is less than 1/10 of that of the SIMS waveguides (b = 1.37).

We have further calculated the spectral width $\delta\lambda_{FWHM}$ and the quality factor Q of the SIMS ring resonator as a function of the coupling ratio k using Eq. (6) – (7),

$$\delta\lambda_{FWHM} = \frac{\lambda_0^2 \arcsin[\frac{1-A^{1/2}}{\sqrt{2(1+A)}}]}{\pi^2 R(N_0 - b\lambda_0) - \lambda_0 \arcsin[\frac{1-A^{1/2}}{\sqrt{2(1+A)}}]} \tag{6}$$

#130097 - $15.00 USD Received 13 Jun 2010; revised 11 Aug 2010; accepted 12 Aug 2010; published 20 Aug 2010

$$Q = \frac{\lambda_0}{\delta\lambda_{FWHM}} \tag{7}$$

where λ_0 = 1.575 μm and A is the loss factor shown in Eq. (1).

The calculated spectral width and the quality factor of the SIMS ring resonators can be found in Fig. 10. As indicated in this pgrahp, when W increases the narrow-band filter characteristics are improved. This effect is further enhanced when k decreases. When W = 230 nm, the utmost values of $\delta\lambda_{FWHM}$ (in Fig. 10(a)) and Q (in Fig. 10(b)) are ≈5 nm and ≈320, respectively. Such highly dispersive and high Q properties make the SIMS based ring resonators unique and will facilitate the development of nanoscale laser cavities, switches and wavelength selective devices.

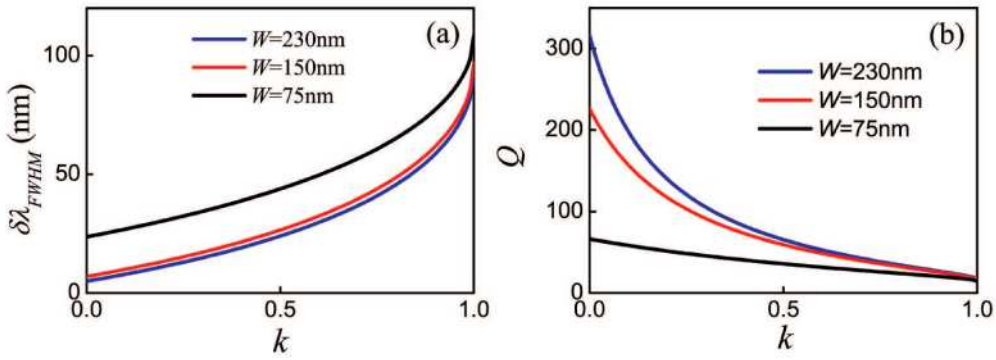

Fig. 10. Spectral width (a) and quality factor (b) for SIMS ring resonators as a function of the coupling ratio k.

6. Suggested fabrication processes

Suggested fabrication processes for the proposed SIMS waveguides and devices mounted on the surface of a silver film are similar to that previously developed. As the minimum line width of these devices is more than 50 nm, these geometries can be fabricated by standard nanolithography techniques [6,22 and 26,]. In the vertical direction, the sandwich layers of the SIMS waveguide can be fabricated using conventional deposition techniques. Deposition of the smooth and high quality layers of insulator film on the top of the silver layer has shown being feasible when the magnetron sputtering technique was used [12].

7. Conclusion

In conclusion, we have proposed and characterized a SIMS waveguide structure for deep sub-wavelength light transport with high intensities and low losses. This waveguide, reconciling the length scale of electronics and optics, possesses a vertical sandwich structure combining a silicon semiconducting strip, a 5-nm thick SiO_2 insulating strip, and a finite-width silver strip on the silver film. This waveguide supports hybrid plasmonic modes with signal transmission over a broadband, tunable dispersion and strong mode confinement. These properties will undoubtedly facilitate the application of SIMS waveguides in integrated optoelectronic systems. To explore such possible integration, the newly proposed SIMS waveguide is used to construct nanoscale plasmonic devices such as directional couplers, bent waveguides and ring resonators. It is demonstrated that these devices, with a functional size of ≈1μm, exhibit considerably low insertion losses and present high photonic performance suitable for optical communications. In addition, we find that light signals with an ultra-high normalized intensity (more than 200 μm^{-2}) can be localized in an optimized ring resonator with R = 500 nm. Our study therefore suggests a great potential of using the proposed SIMS structures for the development of active plasmonic laser cavities, nonlinear electro-optical modulators and optomechanical components for optical communication, sensing and memory processing.

#130097 - $15.00 USD Received 13 Jun 2010; revised 11 Aug 2010; accepted 12 Aug 2010; published 20 Aug 2010

Acknowledgements

This work was supported by NSFC under Grant No. 60977038, NSFC-Research Fund for International Young Scientists under Grant No.60910187, the Scientific Research Foundation of Graduate School of Southeast University under Grant No.YBJJ0925 and Graduate Innovation Program of Jiangsu Province under Grant No. CX09B_050Z.

#130097 - $15.00 USD Received 13 Jun 2010; revised 11 Aug 2010; accepted 12 Aug 2010; published 20 Aug 2010